Cronfa - Swansea University Open Access Repository

_____

This is an author produced version of a paper published in:
Materials & Design

_____

_____

Paper:

http://www.swansea.ac.uk/library/researchsupport/ris-support/

Effects of heat treatment on microstructure and creep properties of a laser powder bed fused nickel superalloy
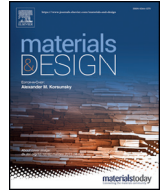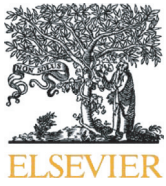
S.J. Davies, S.P. Jeffs *, M.P. Coleman, R.J. Lancaster

Institute of Structural Materials, College of Engineering, Swansea University Bay Campus, Swansea, SA1 8EN, United Kingdom

HIGHLIGHTS

- Adapted Wilshire equations have been used to life variants of Ni-based superalloy C263 produced via laser powder bed fusion
- A method of statistically measuring connectivity of the random boundary network is described and correlated to creep response
- Grain boundary carbides were found to be the dominant strengthening mechanism for improved creep resistance
- Higher temperature solution heat treatments were found to alleviate microstructural anisotropy produced in the LPBF process

GRAPHICAL ABSTRACT
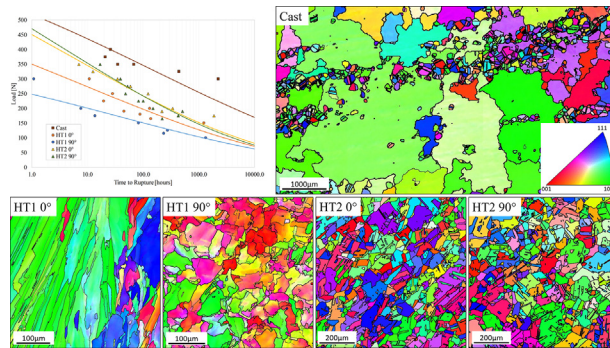
ARTICLE INFO

ABSTRACT

Nickel-based superalloy C263 has been consolidated with Laser Powder Bed Fusion (LPBF) with two perpendicular build orientations and exposed to either of two heat treatment programmes. This study analyses the effects of build orientation and heat treatment on the resulting microstructures produced in LPBF C263 variants, evaluated against a cast equivalent. Results show that although a strongly anisotropic microstructure was present in standard heat-treated (HT1) LPBF material, this was eradicated following an alternate heat treatment regime (HT2) through recrystallisation, aided by high local strain. Subsequently, their mechanical properties have been assessed by means of the Small Punch (SP) creep test. A contrasting presence of $\Sigma 3$ formations was observed between the two LPBF heat treatment programmes with the resulting random grain boundary network (RGBN) revealing shorter potential intergranular crack paths in the HT2 material, although grain boundary carbides were found to be the dominant strengthening mechanism for improved creep resistance. Adapted Wilshire equations have been implemented to predict the long-term creep lives of the C263 variants and their apparent activation energies have been determined.

1. Introduction

Additive manufacturing (AM) is a process that has advanced significantly over the last decade due to its potential for considerable cost benefits in terms of lean manufacture and complex component design for a range of industrial applications. Extensive research has been conducted on a range of AM processes to assess the influence of the process

* Corresponding author.
E-mail addresses: 656258@swansea.ac.uk (S.J. Davies), s.p.jeffs@swansea.ac.uk (S.P. Jeffs), m.p.coleman@swansea.ac.uk (M.P. Coleman), r.j.lancaster@swansea.ac.uk (R.J. Lancaster).

inputs upon structure and properties in metallic components [1,2]. One such process is Laser Powder Bed Fusion (LPBF). Typically, LPBF exhibits features such as epitaxial grain growth promoting textured microstructures parallel to the build direction and in some cases residual stresses due to the high thermal gradients present in the process [3,4]. Post-processing techniques can be applied in an attempt to alleviate some of the residual stresses, anisotropic microstructure and directional properties present after the process, typically through optimised heat treatments [5].

Ni based superalloys are prominently utilised for applications within aerospace and industrial gas turbine engines where good mechanical properties are required at high temperatures. Much of these high temperature properties are derived from γ' precipitates, with superior creep rupture strength influenced by grain boundary carbides [6,7]. In particular, the Ni based superalloy C263 gains a large proportion of its high temperature properties from a fine globular dispersion of Cr-rich $M_{23}C_6$ carbides, typically precipitating following casting or as a result of heat treatments [8]. However, the successful precipitation of this phase following an AM processing route is yet to be determined in this alloy.

Given the anisotropic microstructure and dependence on geometry in the LPBF process, representative mechanical testing of such material can prove difficult. Moreover, the abundance of process parameters exacerbates constraints on the availability of LPBF processed alloys. Therefore, a more feasible option for mechanical testing needs to be applied. The Small Punch (SP) test is a small-scale mechanical test technique involving the biaxial deformation of a miniature disc specimen. Originally developed in the 1980s for remnant life assessments of alloys in the nuclear industry [9], it has since been applied across a wide range of materials, including single crystal nickel alloys [10], steel weldments [11] and intermetallic compounds [12]. The benefits of employing this approach for AM material stems from the ability to test small volumes of material, with the possibility of extracting specimens from discrete locations [12].

The purpose of this study is to evaluate the effects of build orientation and post-process heat treatment on the microstructure of C263 produced via LPBF. Various microstructural considerations have been explored such as grain boundary features and texture through electron microscopy. The influence of microstructural dissimilarities on mechanical performance was assessed with the SP creep test method. In particular, the effect on apparent activation energies for creep across each C263 variant was investigated after applying a modified Wilshire equation lifing approach.

2. Experimental

2.1. Material

Five C263 build variants were the focus of this study. A nominal chemical composition of this alloy is summarised in Table 1. Four LPBF variants were built using an EOS M270 machine from gas atomised powder, with parameters that are broadly in line with industry. However, specific process parameters are considered proprietary. Two were consolidated with a horizontal (0°) build orientation and two with a vertical (90°) build orientation, as illustrated in Fig. 1. Two specimens from each orientation were exposed to either the standard heat treatment programme for C263, HT1 [13], or an experimental heat treatment schedule including a higher temperature solution heat treatment, HT2, as detailed in [14]. This higher temperature was implemented to recrystallise the microstructure and remove the as built texture. Deposition parameters were identical across LPBF builds. Cast

Table 1
Typical chemical composition of C263 (wt%).

	Ni	Co	Cr	Mo	Al	Ti	C	B	Zr
C263	Bal	20.0	20.0	5.9	0.5	2.1	0.06	0.001	0.02

C263, heat treated with HT1 was also examined as part of this study to allow comparisons with LPBF variants. Due to the strong bimodal nature of the cast microstructure and the anisotropic columnar grain structure in the HT1 0° material, the elliptical fit method was used for a more accurate representation of grain size and aspect ratio in these variants. Grain size and aspect ratio measurements of all other variants were collected through the mean linear intercept method. Both methods excluded twin boundaries in recrystallised grain size calculations. Grain data for each C263 type is listed in Table 2.

The LPBF SP specimens were extracted from the threaded ends of conventional test specimens which had been turned to Ø9.5 mm. Cast C263 SP specimens were taken from extruded cylinders, removed from larger sections via wire electrical discharging machining (EDM) as shown in Fig. 1c. In each instance the Ø9.5 mm cylinders were sectioned into approximately 800 μm slices, before being ground by progressively finer silicon carbide abrasive papers to the required specimen thickness of 500 μm ± 5 μm with a 1200 grit finish, in line with the recommendations defined in the European Code of Practice for Small Punch Testing [15].

2.2. Small punch creep test

SP creep tests were performed on a series of high temperature SP creep frames developed at Swansea University, in accordance with the Code of Practice [15]. In this arrangement, the miniature disc specimen is located between an upper and lower die, securely clamping the specimen in place. Loading was typically applied through the central axis of the rig via an upper load pan arrangement, in line with a 2 mm diameter hemispherical ended Nimonic 90 punch. Heat was applied using a single zone digitally controlled furnace and was maintained to within ±1 °C of the test temperature of 780 °C. The temperature was constantly monitored throughout the test by two Type K thermocouples located in a drilled hole in the upper die, close to the surface of the disc. Two linear variable displacement transducers (LVDTs) were utilised at either side of the disc to monitor the displacement; one transducer located below the load pan to measure the displacement upon the top surface of the disc, the other transducer measuring displacement directly from the base of the disc via a quartz rod.

2.3. Microscopy

All microscopy was performed on sectioned and mounted specimens from each C263 variant, polished to a mirror finish. Large scale optical micrographs were captured for each variant and selected areas were scanned using Electron Backscatter Diffraction (EBSD), conducted on a Hitachi SU3500 Scanning Electron Microscope (SEM) operated at 20 kV and 100 μA. Data for grain size, texture, local misorientation and random grain boundary network analyses were collected through EBSD. Carbide micrographs and Energy Dispersive X-ray Spectroscopy (EDS) data for carbide type determination were collected using a JEOL 7800F Field Emission Gun (FEG) SEM and Oxford Instruments SMax 50.

3. Results

3.1. Grain structure & texture analysis

Fig. 2 includes Inverse Pole Figure (IPF) maps for all variants, captured on the transverse plane (TP) as illustrated in Fig. 2a. This plane is orientated normal to the loading direction during SP testing. The IPF map disclosed in 2b highlights the bimodal microstructure apparent in the cast C263 variant; grain measurements for which are reported in Table 2. Bands of finer grains containing Σ3 boundaries sit amongst significantly coarser grains with no special boundaries.

Fig. 2c and d presents the microstructures and crystallographic orientations of the HT1 0° and 90° LPBF variants respectively. Fig. 2c exhibits a strongly anisotropic and elongated microstructure associated
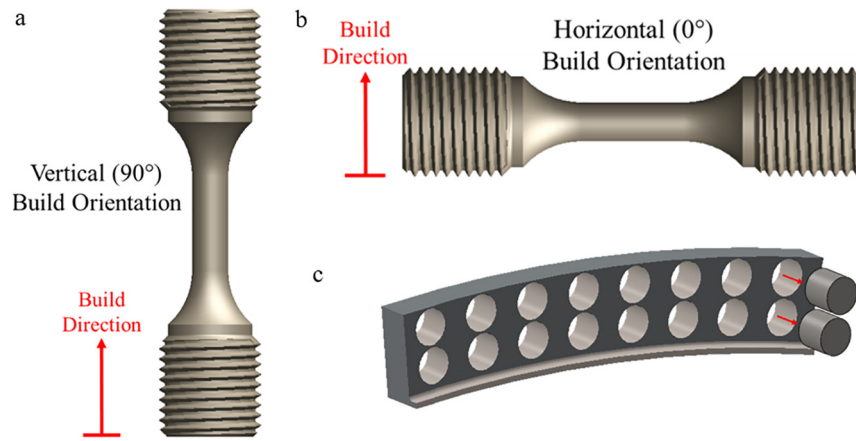
Fig. 1. Schematic showing a) vertical (90°) b) horizontal (0°) LPBF build orientation c) cylinders sectioned from the larger casted ring.

with this heat treatment and build orientation (0°), typical of LPBF consolidated material [1,13]. The 90° counterpart shows a seemingly equiaxed grain morphology perpendicular to the columnar grain length, as shown in Fig. 2d, providing an insight in to the three-dimensional microstructure of HT1 variants. Table 2 provides grain size measurements and, more importantly, grain aspect ratios, used to quantify the extent of elongation in these materials.

Aspect ratios further from 1, associated with HT1 0° C263, and what would be HT1 90° on the longitudinal plane, numerically identify that a columnar grain structure exists. IPF maps and IPFs in Figs. 2c and 3b respectively show that a strong ⟨101⟩ texture parallel to the TP (Z) normal is present in the HT1 0° variant, with HT1 90° builds having a preferential ⟨001⟩ and ⟨101⟩ crystallographic orientation, as shown in Figs. 2d and 3c.

IPF maps for HT2 LPBF variants are displayed in Fig. 2e for the 0° build direction and 2f for the 90° orientation. These two maps of the HT2 material show a more equiaxed microstructure, as seen in the aspect ratios reported in Table 2 of 0.23 and 0.94 for HT1 0° and HT2 0° respectively, as well as a higher proportion of annealing twins. Concomitantly the grains have a smaller average local misorientation spread of 0.19° for HT2 90° compared to 0.47° average kernel average misorientation (KAM) for HT1 90°, Table 2. Both indicate that the higher heat treatment HT2 was successful in recrystallising the as-built columnar microstructure. Fig. 2e and f also shows how recrystallisation has given rise to the abundance of Σ3 annealing twins in HT2 microstructures, comparably with the finer cast grains seen in Fig. 2b, which is reflected in the Σ3 proportions presented in Table 2, e.g. <1% Σ3 proportion for HT1 90° compared to 67.7% Σ3 proportions for HT2 90°. Additionally, Fig. 3 shows a reduced overall texture in both build directions for the HT2 variants, with IPF maxima reducing from 4.64MUD in HT1 0° to 1.92MUD in HT2 0° and from 2.30MUD in HT1 90° to 1.71MUD in HT2 90°.

3.2. Random grain boundary network

For high temperature deformation mechanisms such as creep, it is common for failures to occur in an intergranular manner [16]. Typical defects such as pores and lack of fusion can be found in LPBF materials, which can then have a detrimental effect on mechanical properties [2]. Nevertheless, these features were uncommon in the materials in this study. As such, the grain boundary character is considered as the main parameter for potential crack paths. Interfaces between special boundaries, such as Σ3s and grain boundaries can inhibit intergranular failure by retarding or diverting crack growth [17,18]. The Random Grain Boundary Network (RGBN) may be considered the preferential path for crack propagation where intergranular failure is the dominant mechanism [19,20]. As such the RGBN has been quantified.

EBSD data was used to highlight Σ3 boundaries, selected according to the Brandon criteria [21], on a plain mapped background. ImageJ digital image processing, specifically the 'Find Connected Regions' plugin [22] was used to measure the RGBN through determining the average grain boundary segment length in microns for each sample, as displayed in Fig. 4 and reported in Table 2. The data clearly shows that the cast variant has a larger grain boundary average segment length, 267.3 μm linked to the bimodal nature of the microstructure. The main difference in grain boundary connectivity is between the HT1 (Fig. 4a, b) and HT2 variants (Fig. 4c, d). Both the HT2 0° and 90° samples have shorter random boundary line segments of 17.6 μm and 13.6 μm respectively compared to 86.0 μm and 74.0 μm for HT1 equivalent and is linked to the Σ3 boundary proportions. As a result, the RGBN for HT2 has become more disrupted in comparison to the HT1 samples.

3.3. Local misorientation

It has been discussed that residual stress is commonly manifested in LPBF components; a detrimental characteristic which requires post-process relieving. This has therefore been assessed in terms of internal microstructural strain across all variants, given in Table 2. KAM maps have been produced to provide a visual representation of local misorientation within variant microstructures, translating in to strained regions. These are given in Fig. 5, showing only the 0° orientation for LPBF variants.

The KAM map in Fig. 5a reveals that strained regions lie predominantly within the larger grains of the cast bimodal structure,

Table 2
Average grain size for C263 variants including aspect ratio, average local misorientation and Σ3 length proportion. Random Grain Boundary Network (RGBN) connectivity is reported as well as calculated apparent activation energies from SP creep data.

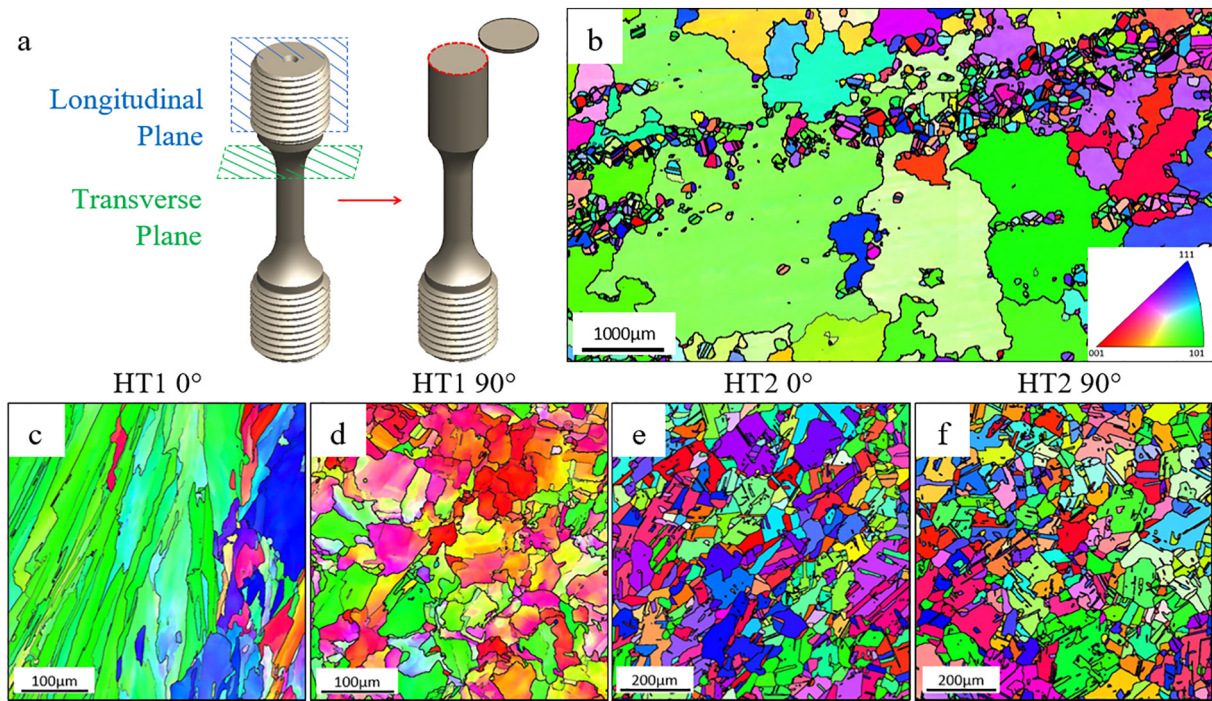| C263 variant	Average grain size [μm]	Aspect ratio	Average KAM [°]	Σ3 [%]	RGBN avg. seg. length [μm]	Apparent activation energy, Q_c^* [kJ·mol^{-1}]
Cast	101.74/921.83	0.55/0.52	0.28	29.0	267.3	175
HT1 0°	29.58	0.23	0.33	0.158	86.0	160
HT1 90°	22.79	0.99	0.47	0.005	74.0	150
HT2 0°	52.02	0.94	0.20	67.6	17.6	140
HT2 90°	57.79	0.94	0.19	67.7	13.6	145

Fig. 2. a) Schematic illustrating uniaxial specimen planes and LPBF SP disc extraction. TP IPF-Z maps of C263 variants; b) cast, c) HT1 0°, d) HT1 90°, e) HT2 0°, f) HT2 90°.

concentrating as horizontal bands. The smaller of the two-grain types contain little indication of local misorientation. The HT1 0° KAM map in Fig. 5b displays an obvious array of local misorientation distributed within all grains of the observed area, averaging at approximately 0.33°. However, Fig. 5c appears to show reduced local misorientation for the HT2 0° variant, with an average of 0.20°.

3.4. Carbides

As a further investigation into grain boundary influences, carbide distribution between C263 build variants has been considered. Micrographs in Figs. 6 and 7 exhibit differences in carbide formation across the material variants. Fig. 6a and b shows clear precipitation of grain boundary carbides in cast C263, with Fig. 6a displaying coarser Ti-MC and Mo-rich M_6C type carbides of various sizes [23]. As expected for cast material, a fine globular dispersion of Cr-rich $M_{23}C_6$ carbides form as discrete particles of approximately 300 nm in diameter at grain boundaries. In contrast, the micrograph of the HT1 variant in Fig. 7a shows little evidence of grain boundary carbides forming. Instead, there appears to be a fine dispersion of Ti and Al segregates suspended in the γ-matrix with an average diameter of <0.1 μm. Whereas HT2 shows evidence of carbide formations (Fig. 7b), mainly of the Ti-MC and Mo-rich M_6C types [23]. Nevertheless, some Ti and Al segregates can still be found within HT2 grains as in HT1 variants.
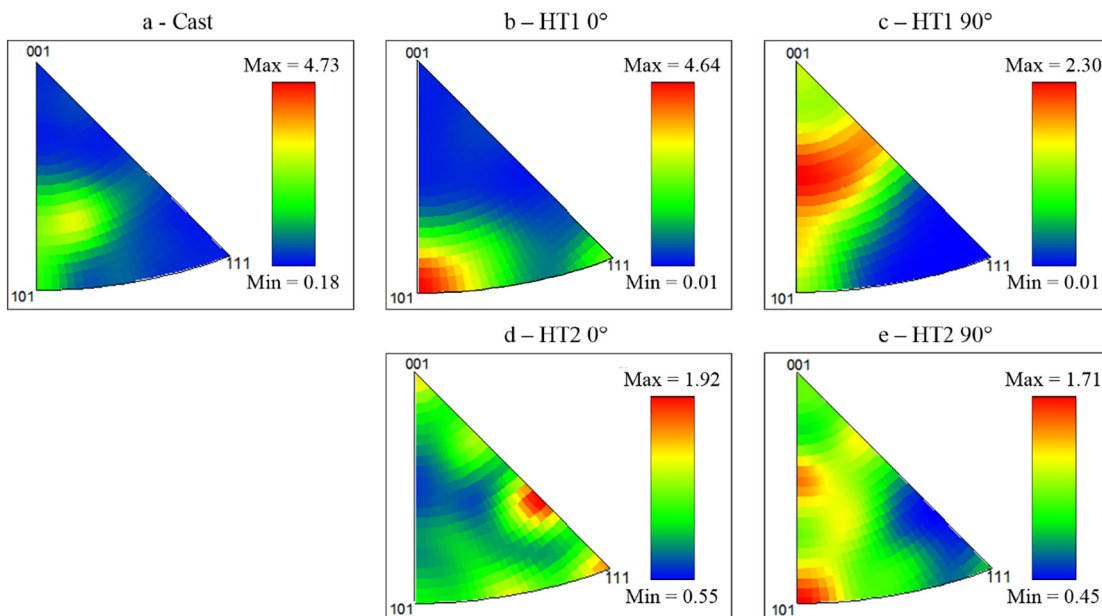

Fig. 3. Z-IPFs of each material variant, corresponding to IPF maps in Fig. 2; a) cast, b) HT1 0°, c) HT1 90°, d) HT2 0°, e) HT2 90°.
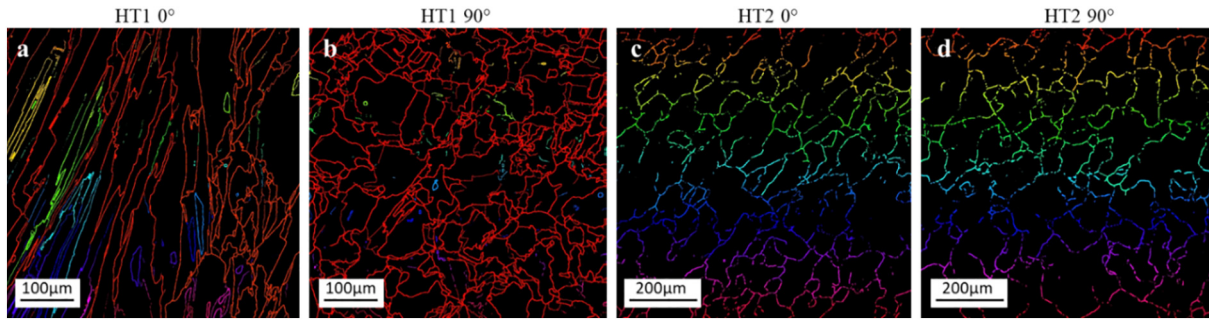
Fig. 4. RGBN connectivity maps for a) HT1 0°, b) HT1 90°, c) HT2 0°, d) HT2 90°. Find connected region images displaying the individual clusters of pixels based on a binary grain boundary network with Σ3 overlaid to disconnect random boundaries so that connected regions are singularly coloured.

3.5. SP creep

Fig. 8 illustrates the experimental data generated for the HT2 0° variant at 780 °C through the SP creep test, showing itself to be an effective method to distinguish the sensitivity of C263 to load at high temperature, with the shortest rupture times for the highest loads. The response is comparable to that from uniaxial creep tests with an initial decaying displacement rate during primary deformation, followed by an accelerating tertiary phase where displacement rate increases until rupture.

The Wilshire equations are a contemporary creep lifing methodology that originates from the assumption that $t_f \rightarrow 0$ as $\sigma \rightarrow \sigma_{TS}$ while $t_f \rightarrow \infty$ as $\sigma \rightarrow 0$ [24]:

$$\frac{\sigma}{\sigma_{TS}} = \exp\left\{-k_1\left[t_f \exp(-Q_c^*/RT)\right]^u\right\} \tag{1}$$

where σ is the applied stress, σ_{TS} is the ultimate tensile stress, t_f is the time to rupture, Q_c^* is the apparent activation energy for creep, R is the gas constant ($8.314 \, \text{J} \cdot \text{mol}^{-1} \cdot \text{K}^{-1}$) and T is the temperature [24]. The parameters Q_c^*, k_1 and u are then derivable from a relatively comprehensive

set of rupture data as is the case here. However, for this research the fundamental Wilshire equation is adapted and normalised through load as opposed to uniaxial stress, meaning $t_f \rightarrow 0$ as $F \rightarrow F_m$ while $t_f \rightarrow \infty$ as $F \rightarrow 0$:

$$\frac{F}{F_m} = \exp\left\{-k_1\left(\left[t_f \exp\left(-\frac{Q_c^*}{RT}\right)\right]^u\right\} \tag{2}$$

where F is the applied load and F_m is the ultimate load from a small punch displacement controlled test. F_m values for these materials are found in the authors' previous work [14]. Fig. 9 presents the load-time to rupture results along with the as-determined fits from the modified Wilshire equations; the apparent activation energies for the alloy variants are given in Table 2.

4. Discussion

4.1. Recrystallisation

IPF maps of LPBF variants in Figs. 2 and 3 have established that complete recrystallisation has been achieved as a result of the higher temperature heat treatment programme (HT2). In order for recrystallisation to occur, an appreciable degree of temperature and deformation is required to activate the process, where the recrystallisation temperature is dependent on the amount of strain already present in the material [25]. KAM data reported in Table 2 show that local misorientation is noticeably reduced in HT2 C263 compared to the HT1 microstructure. Therefore, it has been established that the deformation present in HT1 is an additional driving force for recrystallisation, in line with previous research [25]. Fig. 5a is illustrative of this phenomenon, as congregations of finer recrystallised grains in the cast microstructure follow bands of high local misorientation. Furthermore, these grains also contain little deformation as this strain has been relieved, or contributed to recrystallisation, as is the case in LPBF variants.

4.2. Random grain boundary network variation

The majority of recrystallised grains in cast and HT2 variants contain annealing twins (Σ3s). Increasing Σ3 proportions has been shown to improve grain boundary sensitive properties by becoming incorporated into the random boundary network and acting to impede the transport of cracks along it [17]. This has led to the use of the connectivity of the RGBN as a measure of the degree of disconnection of the higher angle grain boundaries. However, a quantitative method for reporting RGBN connectivity has yet to be agreed upon. Therefore, an image processing methodology is described in Section 3.2. The average RGBN segment lengths, reported in Table 2 and shown in Fig. 4, reveal that the increase in Σ3 proportions between the HT1 and HT2 microstructures has resulted in a reduction of RGBN average section length from 86 μm for HT1 0° to 17.6 μm for HT2 0° for example. Therefore, crack propagation
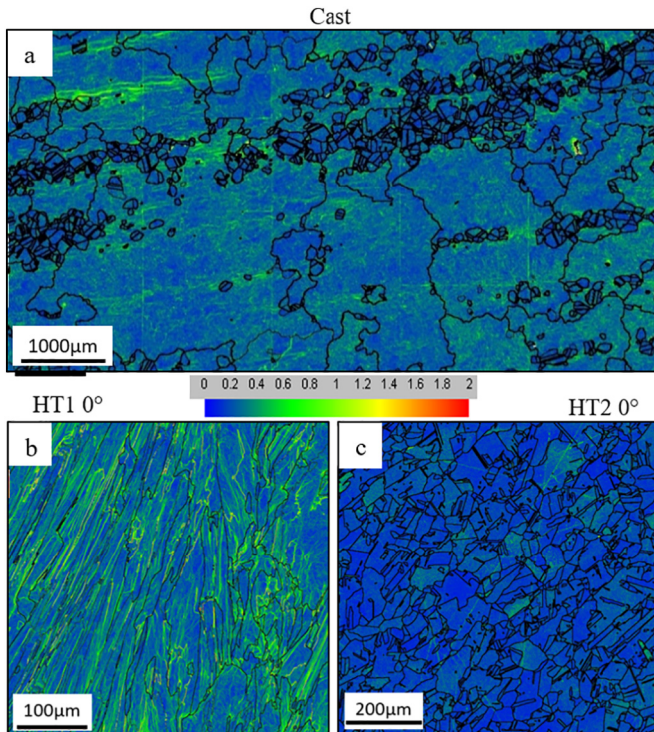

Fig. 5. Local KAM maps showing high local misorientation spread for the cast and HT1 0° samples and a much lower local misorientation spread for HT2 0°.
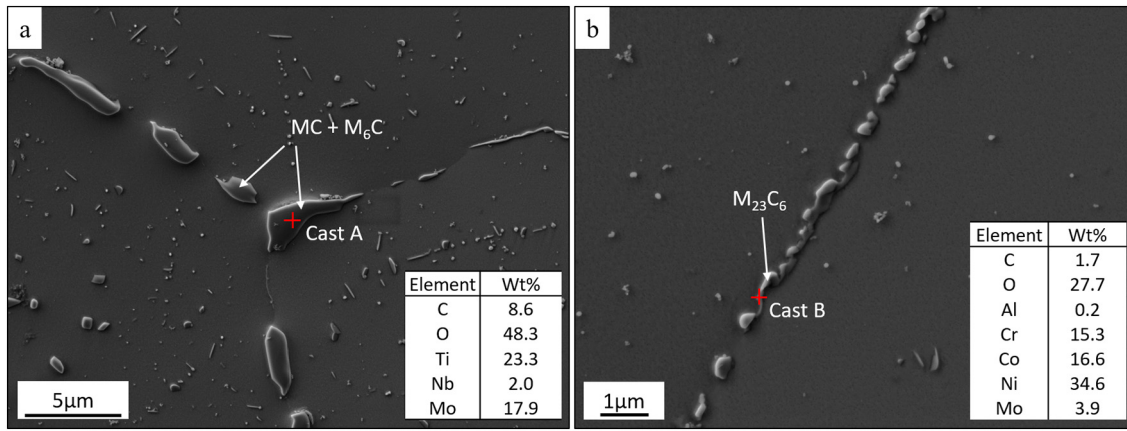
Fig. 6. Micrographs and elemental analysis of carbide formations in cast C263 a) coarser M_6C type carbides b) fine globular Cr-rich $M_{23}C_6$ type carbides.

would be more difficult for a more disconnected random boundary network such as those in HT2 samples. This is supported by the creep data shown in Fig. 9 where the two HT2 samples show a higher load required for similar rupture times compared to the HT1 material.

4.3. Carbide morphology and distribution

Carbide distribution has been considerably influenced by the processing route and heat treatment of C263. Carbides found in cast C263, as in Fig. 6a and b, do not appear in HT1 LPBF variants, even though the same heat treatment has been applied, alternatively leaving a fine dispersion of Ti and Al segregates suspended in the γ-matrix. $M_{23}C_6$ and M_6C carbides typically precipitate from the breakdown of coarser MC carbides [23]. MC carbides largely form during the melt of a given process or as a result of high temperatures in a supersaturated solid solution [23]. In the case of LPBF, the rapid heating and solidification [2,3] would limit the time at liquidus compared with a casting process, narrowing the window for MC carbides to form, rendering limited opportunity for the precipitation of other carbide types. The Ti and Al segregates have likely formed as a result of microsegregation in interdendritic regions from the rapid solidification process [4,25]. In HT2 variants, MC and M_6C carbides have precipitated. The higher temperature solution heat treatment for these variants have encouraged the growth of MC carbides from what is likely a supersaturated solid solution, developing in to M_6C carbides following ageing. The higher temperature heat treatment has also resulted in a reduction in Ti and Al segregates by dissolving them in the γ-matrix by solid-state diffusion or by their reaction to contribute to MC carbides.

4.4. SP creep: influence of microstructure, carbides and apparent activation energies

Fig. 8 shows the SP creep results for the C263 alloy variants with the cast material displaying the greatest resistance to creep loading. HT2 variants exhibit a significantly reduced resistance although similar to one another, followed by a further reduction in HT1 0° and finally the least resistance shown by HT1 90°. This trend is supported by the microstructural analysis in terms of grain size, texture, RGBN and carbide formations.

The role and influence of carbides has previously been controversial [7] although it is accepted that high temperature creep properties improve with the presence of carbon where the formation of carbides at grain boundaries is likely. This research corroborates this perception, with a large increase in rupture strength observed for cast material where there are clear grain boundary carbide precipitates ($M_{23}C_6$), in comparison to the LPBF alloys where little or no $M_{23}C_6$ carbide formations are present to inhibit grain boundary deformation. The scatter observed in the cast properties is understood to be due to the bimodal microstructure and the sensitivity of the small specimen test size meaning the number and type of grains being tested could be considerably different.

Examining the LPBF material performance reveals the HT1 90° variant ranks lowest; this is recognised as a combination of the smallest grain size and the relative absence of carbides and Σ3 type boundaries. The improvement seen in the HT1 0° variant is believed to be due to a slight increase in grain size and an aspect ratio further from 1. In the SP test, deformation occurs in a biaxial manner, causing membrane stretching across the transverse plane [26], in directions parallel and
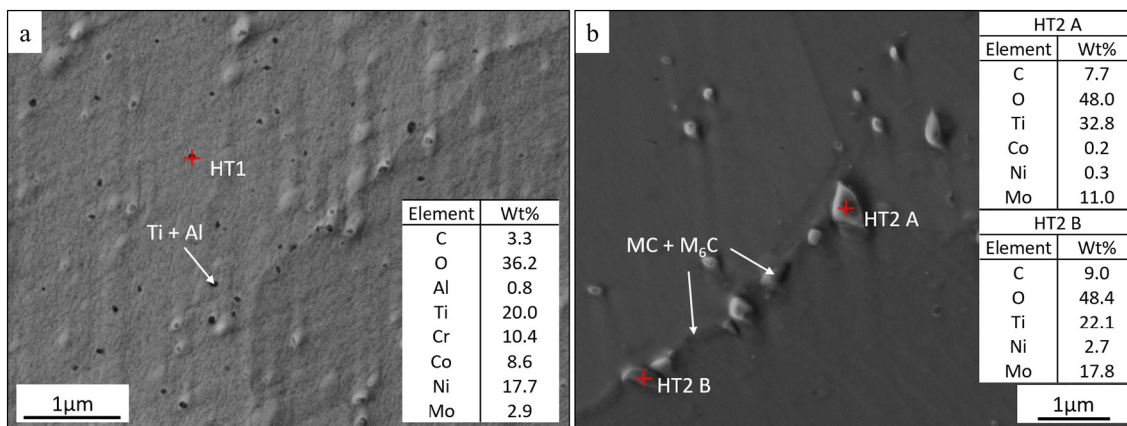

Fig. 7. Micrographs and elemental analysis of carbide and other precipitation formations in LPBF C263 variants a) HT1 0° b) HT2 0°.
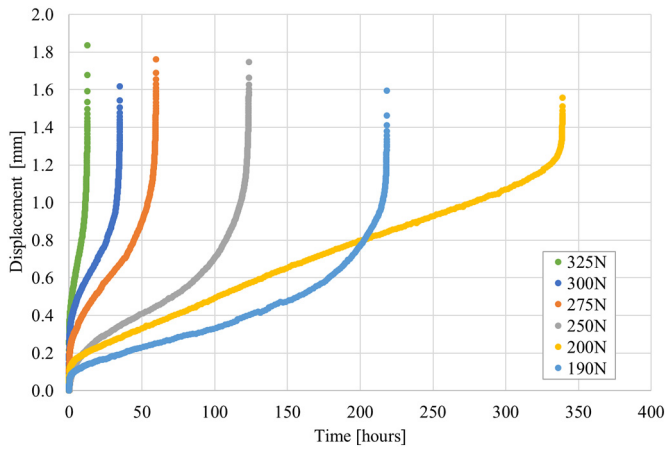
Fig. 8. Small punch creep displacement-time curves for HT2 0° variant at 780 °C over a range of loading conditions.

perpendicular to the columnar grain alignment in the HT1 0° variant. Therefore, the probability of intercepting a grain boundary is reduced, thus improving resistance to creep parallel to the columnar grain structure.

It has been shown that Σ3 type boundaries can act to retard or deflect crack growth so it would be expected that the HT2 materials would demonstrate better creep properties compared to HT1 material, with over 67% length Σ3 type boundaries. The result of this is a large reduction in the RGBN average segment length from 74–86 μm in HT1 to 13.6–17.6 μm in HT2. The scale of which these Σ3 boundaries, and the resulting RGBN act to improve properties is clear with the near order of magnitude increase in rupture life between HT1 and HT2 as shown in Fig. 8. The SP creep life of HT2 0° and HT2 90° is found to be very similar, although with values of grain size, aspect ratio, Σ3 and RGBN lying closely to one another, this is expected. Nonetheless, it demonstrates that the experimental heat treatment schedule with a higher temperature solution heat treatment has largely alleviated microstructural differences and improved mechanical properties in terms of creep resistance when compared to HT1.

Overall, based on the microstructural analysis and SP creep results it is suggested that the influence of carbide formations on rupture life is found to be more prominent than the retardation caused by Σ3 type boundaries due to the vast difference between cast and HT2 materials, although both act to improve creep properties. However, the bimodal grain structure in the cast material and its contribution to the scatter in the results in these small sample size tests must be considered.
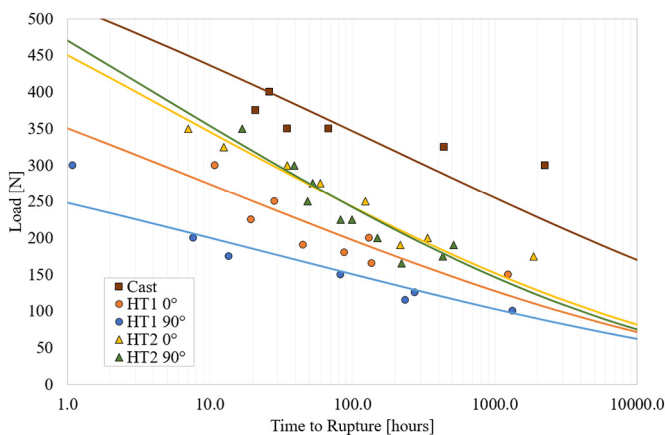

Fig. 9. Load vs. time to rupture for the variants of C263 along with the modified Wilshire equation predictions.

In determining the constants for the adapted Wilshire equations for these materials, in the first instance a value of activation energy, Q_c^*, must be employed. The activation energy for self-diffusion (Q_{SD}) in polycrystalline nickel alloys is typically considered to be ~300 kJ·mol^{-1} [16]. The mechanical characterisation carried out in this research through SP creep revealed grain boundary deformation to be the dominant mechanism in these variants, thus providing preferential diffusion along these favoured paths, which in turn results in an activation energy of $Q_c^* = 0.5Q_{SD}$. Through plotting $[t_f \cdot \exp(-Q_c^*/RT)]$ against $\ln[-\ln(F/F_m)]$ constants u and k_1 were easily determined for the best fit ($R^2 = 0.88$), with a range of apparent activation energies, $Q_c^* = 140$–175 kJ·mol^{-1} as given in Table 2, all of which sensibly fall in the region for preferential diffusion. The differences in these Q_c^* values are thought to be attributed to the variant microstructures, specifically boundary densities which likely have a significant role in these miniaturised tests. For instance, the cast material will have a relatively low boundary density, particularly in regions of the larger grains, resulting in the highest apparent Q_c^*. While the HT1 variants have the smallest grain size and therefore the highest grain boundary density, the increase in grain size in the HT2 variants is coupled with an abundance of special boundaries meaning HT2 variants have the highest overall boundary density thus producing the lowest apparent Q_c^*. Overall, the high R^2 values produced through this approach suggests that the Wilshire equations are an effective tool for predicting creep life in these advanced materials.

5. Conclusions

In this study, an in-depth analysis of five C263 variants was conducted to determine the influence of heat treatments on their microstructures and mechanical properties. Advanced microscopy methods as well as the SP creep test have been utilised and the following conclusions have been drawn:

- The SP creep test has successfully ranked the high temperature mechanical performance of C263 build variants, with adapted Wilshere equations effectively determining the long-term creep lives and apparent activation energies.
- The higher temperature solution heat treatment in HT2 has successfully alleviated microstructural anisotropy by reducing texture and the columnar grain structure in LPBF variants. The higher temperature combined with the high degree of local misorientation evident in HT1 provides an additional driving force for recrystallisation and twinning.
- Random Grain Boundary Networks reveal shorter potential intergranular crack paths in HT2 variants as a result of Σ3 boundaries, further strengthening their resistance to creep deformation.
- The presence of grain boundary carbides acts to significantly improve the creep resistance of the cast material, and has been revealed as the dominant strengthening mechanism considering the RGBN is found to be larger than in all LPBF material variants.

Author contribution

The research presented in this paper was carried out as a collaboration between all authors. The research theme was defined by Robert Lancaster, Spencer Jeffs, Mark Coleman and Sean Davies. Sean Davies and Mark Coleman performed the SEM and EBSD analysis. Spencer Jeffs performed the mechanical testing. Sean Davies, Spencer Jeffs, Mark Coleman and Robert Lancaster co-worked on the discussion and interpretation of the results with respect to the material's microstructure. All authors have contributed to, edited and approved the final manuscript.

The raw/processed data required to reproduce these findings cannot be shared at this time as the data also forms part of an ongoing study.

References

[1] T. DebRoy, H.L. Wei, J.S. Zuback, T. Mukherjee, J.W. Elmer, J.O. Milewski, A.M. Beese, A. Wilson-Heid, A. De, W. Zhang, Additive manufacturing of metallic components – process, structure and properties, Prog. Mater. Sci. 92 (2018) 112–224.

[2] J.J. Lewandowski, M. Seifi, Metal additive manufacturing: a review of mechanical properties, Annu. Rev. Mater. Res. 46 (2016) 151–186.

[3] X. Song, M. Xie, F. Hofmann, T. Illston, T. Connolley, C. Reinhard, R.C. Atwood, L. Connor, M. Drakopoulos, L. Frampton, A.M. Korsunsky, Residual stresses and microstructure in Powder Bed Direct Laser Deposition (PB DLD) samples, Int. J. Mater. Form. 8 (2015) 245–254.

[4] G.P. Dinda, A.K. Dasgupta, J. Mazumder, Texture control during laser deposition of nickel-based superalloy, Scr. Mater. 67 (2012) 503–506.

[5] E. Chlebus, B. Kuźnicka, T. Kurzynowski, B. Dybała, Microstructure and mechanical behaviour of Ti-6Al-7Nb alloy produced by selective laser melting, Mater. Charact. 62 (2011) 488–495.

[6] T.M. Pollock, S. Tin, Nickel-based Superalloys for advanced turbine engines: chemistry, microstructure and properties, J. Propuls. Power 22 (2006) 361–374.

[7] R.C. Reed, The Superalloys: Fundamentals and Applications, first ed. Cambridge University Press, Cambridge, 2006.

[8] I.S. Kim, B.G. Choi, H.U. Hong, J. Do, C.Y. Jo, Influence of thermal exposure on the microstructural evolution and mechanical properties of a wrought Ni-base superalloy, Mater. Sci. Eng. A 593 (2014) 55–63.

[9] M.P. Manahan, A.S. Argon, O.K. Harling, The development of a miniaturized disk bend test for determination of post irradiation mechanical properties, J. Nucl. Mater. 104 (1981) 1545–1550.

[10] S.P. Jeffs, R.J. Lancaster, T.E. Garcia, Creep lifing methodologies applied to a single crystal superalloy by use of small scale test techniques, Mater. Sci. Eng. A 636 (2015) 529–535.

[11] S. Yang, X. Ling, Y. Zheng, R. Ma, Creep life analysis by an energy model of small punch creep test, Mater. Des. 91 (2016) 98–103.

[12] R.C. Hurst, R.J. Lancaster, S.P. Jeffs, M.R. Bache, The contribution of small punch testing towards the development of materials for aero-engine applications, Theor. Appl. Fract. Mech. 86 (2016) 69–77.

[13] T. Vilaro, C. Colin, J.D. Bartout, L. Nazé, M. Sennour, Microstructural and mechanical approaches of the selective laser melting process applied to a nickel-base superalloy, Mater. Sci. Eng. A 534 (2012) 446–451.

[14] S. Davies, S. Jeffs, R. Lancaster, G. Baxter, High temperature deformation mechanisms in a DLD nickel superalloy, Materials 10 (2017) 457.

[15] CEN Workshop Agreement CWA 15267, European Code of Practise: Small Punch Test Method for Metallic Materials, 2007.

[16] A. Manonukul, F.P.E. Dunne, D. Knowles, Physically-based model for creep in nickel-base superalloy C263 both above and below the gamma solvus, Acta Mater. 50 (2002) 2917–2931.

[17] V. Randle, G. Owen, Mechanisms of grain boundary engineering, Acta Mater. 54 (2006) 1777–1783.

[18] T. Watanabe, Grain boundary design for desirable mechanical properties, Le J. Phys. Colloq. 49 (1988) (C5-507-C5-519).

[19] V. Randle, M. Coleman, G. Owen, Evolution of the grain boundary network as a consequence of deformation and annealing, Mater. Sci. Forum 550 (2007) 35–44.

[20] S. Holland, X. Wang, X.Y. Fang, Y.B. Guo, F. Yan, L. Li, Grain boundary network evolution in Inconel 718 from selective laser melting to heat treatment, Mater. Sci. Eng. A 725 (2018) 406–418.

[21] D.G. Brandon, The structure of high-angle grain boundaries, Acta Mater. 14 (1966) 1479–1484.

[22] J. Schindelin, I. Arganda-Carreras, E. Frise, V. Kaynig, M. Longair, T. Pietzsch, S. Preibisch, C. Rueden, S. Saalfeld, B. Schmid, J.-Y. Tinevez, D.J. White, V. Hartenstein, K. Eliceiri, P. Tomancak, A. Cardona, Fiji: an open-source platform for biological-image analysis, Nat. Methods 9 (2012) 676–682.

[23] M.J. Donachie, S.J. Donachie, Superalloys: A Technical Guide, second ed. ASM International, Materials Park, 2002.

[24] B. Wilshire, P.J. Scharning, Long-term creep life prediction for a high chromium steel, Scr. Mater. 56 (2007) 701–704.

[25] F.J. Humphreys, M. Hatherly, Recrystallisation and Related Annealing Phenomena, second ed. Elsevier Ltd, 2004.

[26] M. Coleman, H. Alshehri, R. Banik, W. Harrison, S. Birosca, Deformation mechanisms of IN713C nickel based superalloy during small punch testing, Mater. Sci. Eng. A 650 (2016) 422–431.